Progress In Electromagnetics Research B, Vol. 82, 73–92, 2018

Multilayer Structural Diagnosis with Quasi-3D Microwave Imaging Using Ultrawideband Radio Frequency Noiselet Waveforms

Tae Hee Kim and Ram M. Narayanan*

Abstract—Microwave radar imaging is increasingly being used in infrastructure monitoring applications due to its low cost, rapid measurement time, non-contact characteristics, and ability to penetrate nonmetallic media. An appropriate waveform design must be designed to obtain accurate information on the targets observed or the features being probed. Ultrawideband (UWB) radio frequency (RF) noiselets are excellent candidate waveforms in view of their multiresolution and interference rejection features. In this paper, a waveform optimization approach for UWB noiselet waveforms is described to achieve high peak-to-sidelobe ratio (PSLR) to enhance imaging capabilities. Synthetic aperture radar (SAR) scanning for microwave imaging is introduced after analyzing the essential microwave approaches for the multilayered structure. Image reconstruction using SAR scanning is performed for various multilayered structures and quasi-3D images of these structures are presented for nondestructive testing and evaluation (NDT&E) applications.

1. INTRODUCTION

Noise waveforms have been studied in radar applications during the past several decades due to several desirable properties, such as low probability of detection and interception (LPD & LPI), and suppression of interference and signal jamming [1, 2]. Noise radar advances in signal and image processing are shown to achieve multidimensional representation for target detection with relatively simple designs in algorithms and hardware. Applications of noise radar systems include ground penetrating radar (GPR), through-the-wall radar (TWR), and synthetic aperture radar (SAR) [3–5].

Ultrawideband (UWB) radio frequency (RF) noiselet waveforms are noise signals with wideband frequency content which are designed as short duration pulsed waveforms containing high frequency random signals within the operating frequency bandwidth [6]. They can also be considered as a frequency modulated (FM) random waveform since the waveforms are modulated with signals at random frequencies. The noiselet, introduced recently, possesses a sparse representation and is composed of random noise coefficients [7]. As a pulsed "noisy" wavelet, it is perfectly uncorrelated to the signal representation of wavelets. Thus, noiselets have the potential of higher probability of signal detection and recovery from sparse data [7, 8].

Microwave radar imaging, in specific, is one beneficiary of applying UWB RF noiselet waveforms, since higher image resolution is desired to detect small defects and anomalies. The typical radar system radiates the RF signal from the transmitter while the receiver captures the scattered fields which are related to the electrical properties of the target media. The range resolution of an FM radar system, ΔR, is inversely proportional to the transmit bandwidth, Δf, by employing matched filtering or correlation processing [9]. Moreover, the random nature of the noiselet waveform over a wide frequency band is advantageous to explore the spatial neighborhood around the nominal detection range. UWB RF noiselets, therefore, are promising waveforms for microwave and radar applications.

Received 29 August 2018, Accepted 25 September 2018, Scheduled 4 October 2018
* Corresponding author: Ram M. Narayanan (ram@engr.psu.edu).
The authors are with the Department of Electrical Engineering, The Pennsylvania State University, University Park, PA 16802, USA.

2. UWB RF NOISELET WAVEFORM AND APPROACH

2.1. Generation of Noiselet Waveform for Computation and Optimization

UWB RF noiselet, in general, can be defined as a waveform created through the amplification of thermally generated noise and subsequent filtering over the desired operating frequency band. For numerical analysis and simulations, it is necessary to form a discrete and digitized version of the UWB RF noiselet. A noiselet waveform is formed from a Gaussian distributed random process and can be expressed as

$$x\left(N,t\right)=\sum_{i=1}^{N}\left[x_I(i)+jx_Q(i)\right]\exp(j2\pi f_c(i)t) \tag{1}$$

where $x_I(i)$ and $x_Q(i)$ are the random Gaussian coefficients obtained from $\mathcal{N}(0,\sigma^2)$ over the operating frequency range given by $f_c(i)\in[f_{\min},f_{\max}]$, and N is the number of samples [10]. The bandwidth $\Delta f=f_{\max}-f_{\min}$. Fig. 1 shows a sample UWB noiselet waveform in both the time and frequency domains depicting the amplitude and power spectral density over X-band (8 to 12 GHz).

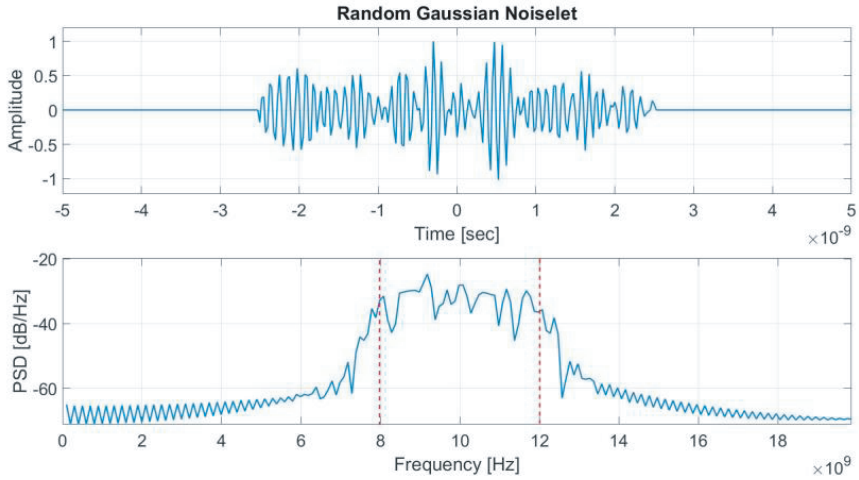

Figure 1. A sample random Gaussian noiselet waveform generated with 400 sample amplitudes ($N=400$) drawn from $\mathcal{N}(0,\sigma^2)$ with a pulse duration of 5 nsec and a frequency band of 8–12 GHz.

While a UWB noiselet described above shows potential for target detection and feature imaging, it is seen that waveform crafting and optimization are required to achieve more accurate results. Due to its randomness for each realization, the obtained peak-to-sidelobe ratio (PSLR) is not always adequate to suppress reflections from ranges other than the desired value. Fig. 2 provides examples of matched filtering results using four different noiselet realizations in a noisy test environment by adding arbitrary additive uncorrelated white Gaussian noise for detecting target interfaces located at 10 cm and 12 cm. While Fig. 2(a) shows an optimal noiselet waveform using which the interfaces are clearly detected, Figs. 2(b)–2(d) show inadequate detection performance, such as the occurrence of peaks where there are no interfaces, higher reflection from the second interface compared to the first, and occurrence of false alarms. It is believed that these unwanted peaks are due to low PSLR values which accentuate signals at unwanted ranges.

PSLR is defined as the ratio formed by the mainlobe intensity to the highest sidelobe intensity of the matched filtered output and is expressed as

$$\mathrm{PSLR}=\frac{I_{\mathrm{main}}}{I_{\mathrm{side}}} \tag{2}$$

where I_{side} and I_{main} stand for the maximum intensities of sidelobe and mainlobe, respectively. In case of a specific target or specimen, the trial matched filtering via searching for a reflection peak from the

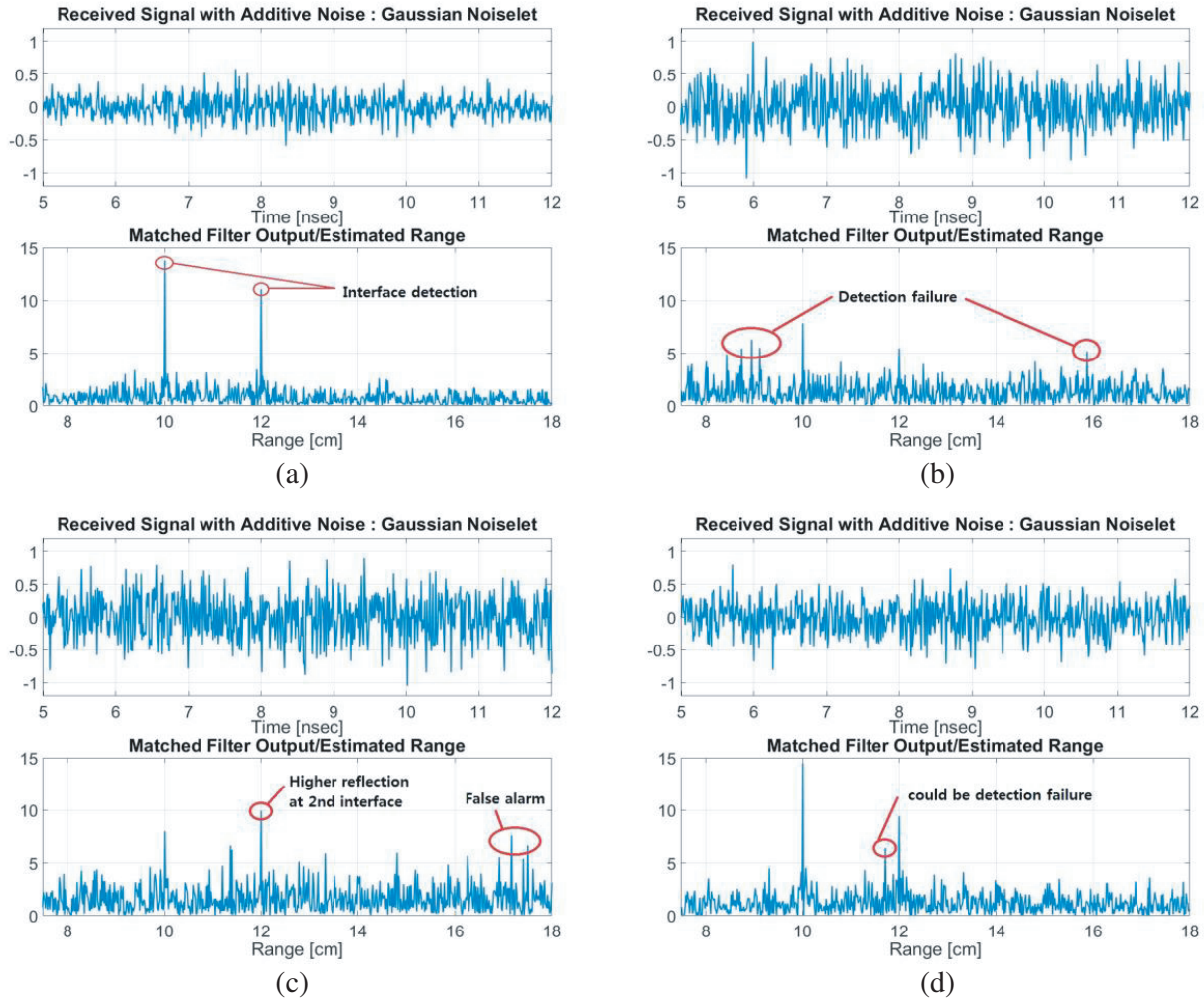

Figure 2. Matched filtering results comparing noiselet waveform realizations for target interfaces located at 10 cm and 12 cm from sensor. Arbitrary random noise is added to the received signal to model a noisy testing environment. These results show four sample cases from 100 iterations: (a) excellent detection, (b) detection failure, (c) insufficient reflection from first interface, and (d) possibility of a false alarm.

first interface of test specimen will provide the decision of optimal waveform since the standoff distance between the sensor and test specimen is already determined. Signals with lower PSLR would result in the faulty detection and/or target masking which will cause false alarms from the target [11].

Figure 3 shows the histograms of the peak intensity value of mainlobe and the peak intensity value of sidelobe, while Fig. 4 shows the histogram of the PSLR. These histograms are formed using 100 sample iterations of the noiselet waveform generation. Each realization is evaluated based on the trial and error measurements of the final image correlation factors. Such a scheme for PSLR optimization has also implemented experimentally showing excellent results by proper choice of the noiselet waveform [12].

In order optimize the noiselet waveform, the procedure depicted in Fig. 5 is implemented. To determine the optimal noiselet waveforms, a PSLR value less than 2.5 is defined as causing false alarms based on various trials on image data reconstruction. A peak intensity of mainlobe less than 10.0 is considered as a non-optimal noiselet waveform. In addition, the failure of optimized noiselet waveform will be judged if any sidelobe intensity exceeds the value of 5.0. These values are determined during the process of image reconstruction which will be introduced in later sections.

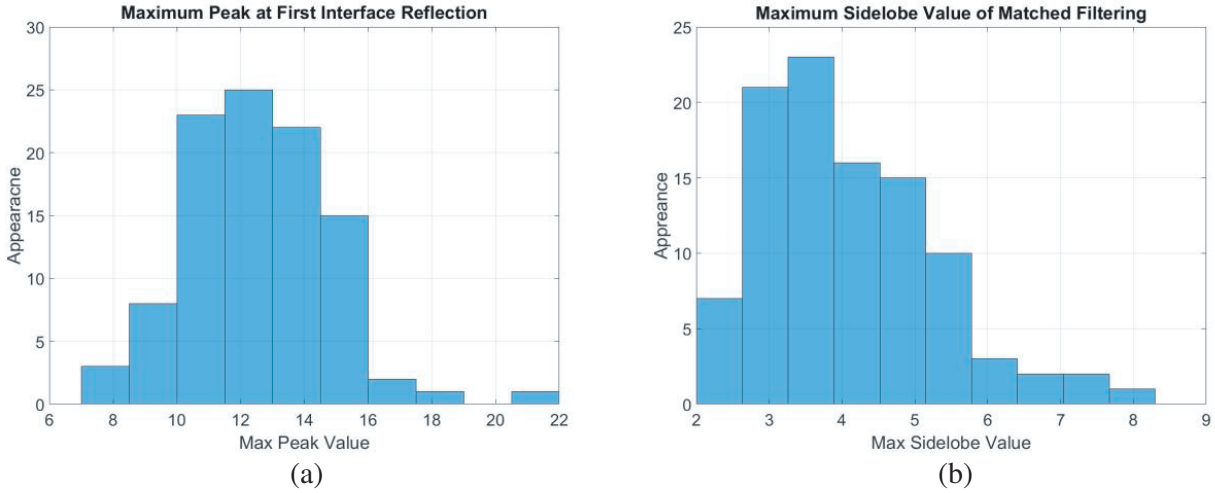

Figure 3. (a) Maximum peak intensity of mainlobe, and (b) maximum sidelobe intensity from 100 iterations of the noiselet generation.

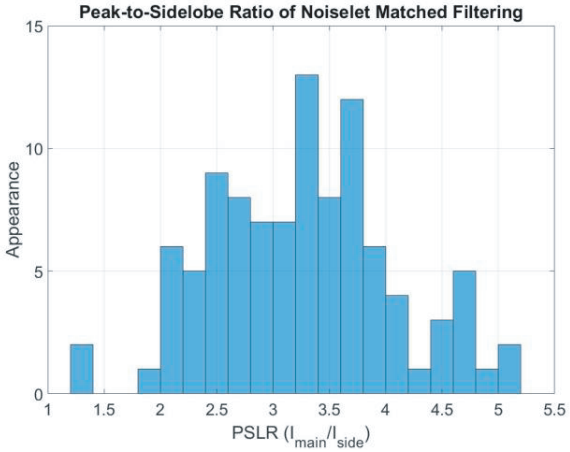

Figure 4. Peak-to-sidelobe ratio (PSLR) from 100 iterations of the noiselet generation.

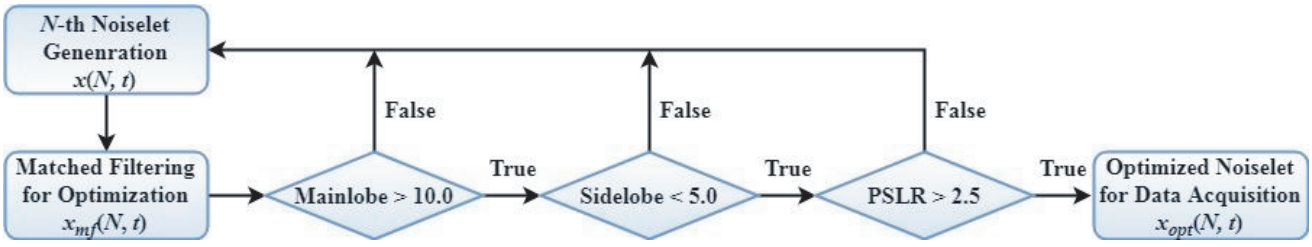

Figure 5. Optimization procedure for generating useful noiselet waveforms with the appropriate conditions for peak values and PSLR to avoid false alarms or flawed detections.

3. STRUCTURAL DELAMINATIONS AND ELECTROMAGNETIC APPROACHES

3.1. Delaminations in Multilayer Fiber Reinforced Structures

Fiber reinforced plastic or polymer (FRP) composites are materials designed to achieve higher strength and lighter weight with fabricated fibers into an epoxy matrix. FRP composites are widely used as

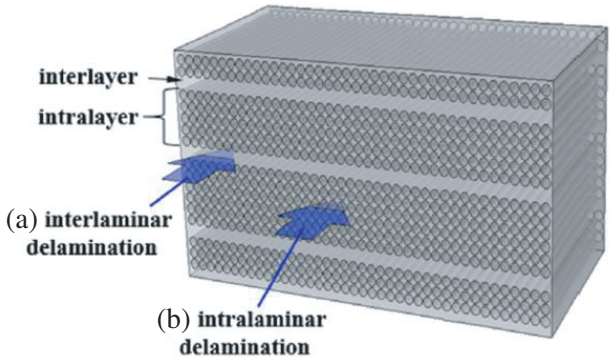

Figure 6. Structure schematics of (a) interlaminar and (b) intralaminar delamination in laminated unidirectional FRP composite materials.

structural materials in aircrafts, automobiles, vehicles, and constructed structures. However, these composite materials also have disadvantages due to their structural matrix form in that the strength of the structure decreases rapidly with the presence of internal defects. These defects can negatively impact the service life of the structure. Thus, it is necessary to define the inner defects by exploring the manufacturing process of FRP composite structures which are formed by laminations. Defects at the time of manufacture include porosity, delaminations, presence of foreign materials, disbonds, cracks, and wrinkles, while those in service include delaminations, disbonds, cracking, moisture ingress, and heat damage [13]. For example, delaminations can be classified as interlaminar and intralaminar as shown in Fig. 6 [14].

Most FRP structures are composed of unidirectional or woven fiber layers and these delaminations are susceptible to the formation of microscale damage such as interfacial debonding, matrix cracking, fiber breakage, and delamination. One or more delaminations initiated in the composite can ultimately lead to final failure of the material. Thus, monitoring of damage initiation and propagation in fiber-reinforced composites is of significant interest for in-service monitoring of structures. Defects in the form of cracks that lie perpendicular to the direction of applied loads are particularly detrimental to the strength and durability of composites [15]. Transverse cracking occurs in the 90° plies of cross-ply laminates at strains much lower than the ultimate failure strain. The spacing of transverse cracks is dependent on the thickness of the transverse ply and the applied stress [16]. Thinner 90° layers have higher constraint due to the adjacent stiff 0° layers and show crack initiation at higher strains and a larger saturation density of cracks before failure [17]. Therefore, it is necessary to monitor the initial delamination and its deformation using an appropriate nondestructive testing scheme, such as the one described in this paper using electromagnetic waves or microwaves.

Addressing the actual delaminations on FRP composite structures, Fig. 7 depicts defects caused due to hygrothermal environment [18]. It provides cross-sectional images showing the difference between unidirectional FRP samples without delaminations and with delaminations after immersing in water at 80°C for 6 months. It was noted that delaminations occurred in lateral directions within the range of

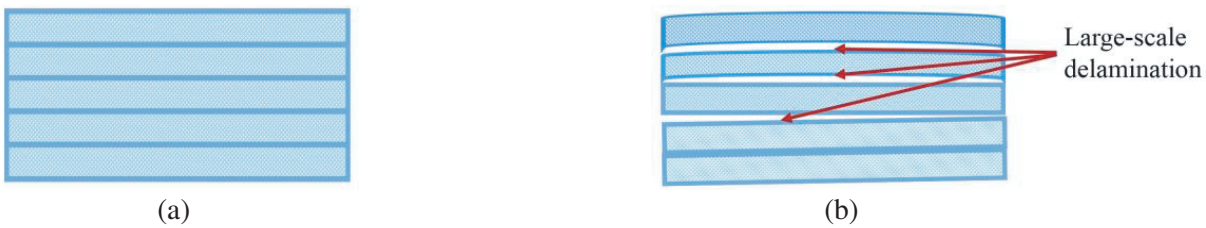

Figure 7. Cross-sectional views of unidirectional FRP laminated composites. (a) Sample with no delamination, and (b) sample immersed in water at 80°C for 6 months resulting in interlaminar delamination.

(a) (b)

Figure 8. Cross-sectional views showing ply swelling due to interlaminar stress. (a) Interlaminar shear stress a result of moisture uptake, and (b) combined effects of interlaminar shear stress and swelling resulted from moisture absorption.

centimeters; thus these structural characteristics of delaminations are investigated using our approach for both scale and depth detection.

Delaminations can also be caused by moisture uptake in FRP laminates [18]. Interlaminar shear stress appear when the adjacent plies are ready to expand along different directions as a result of moisture uptake, as shown in Fig. 8. The ply is then forced out under the combined effects of interlaminar shear stress and swelling resulted from moisture absorption.

In addition, damages caused by bird hits and hail impact at speeds of 100–250 m/s, when in service, can result in warping on the order of 7–10 mm at the point of impact, and subsequent delaminations [19].

3.2. Electromagnetic Waves Traveling in FRP Interfaces

Figure 9 depicts the geometry of a typical interface between two media and shows the forward and reflected electric fields, as well as the reflected and transmitted electric fields in both directions.

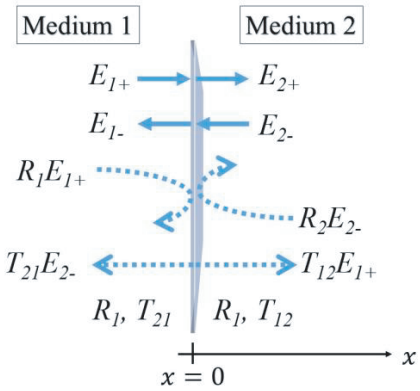

Figure 9. Schematic diagram of traveling waves on the interface between two dielectric media of incident, reflected, and transmitted electric fields.

The wave propagation matrix is created to form the basis matrix for extension to multilayer interfaces. For a wave incident on the interface from Medium 1 ($x < 0$), the reflection coefficient R_1 is defined as

$$R_1 = \frac{E_{01}^r}{E_{01}^i} \tag{3}$$

where E_{01}^r and E_{01}^i are the reflected and incident electric fields in Medium 1, respectively, at $x = 0$. Similarly, the transmission coefficient T_{12} is defined as

$$T_{12} = \frac{E_{02}^t}{E_{01}^i} \tag{4}$$

where E_{02}^t is the amplitude of the transmitted wave in Medium 2. Both reflection and transmission coefficients are related as $1 + R_1 = T_{12}$. These coefficients, then, can be expressed in terms of the

intrinsic impedances of Medium 1 and Medium 2, Z_1 and Z_2 respectively, as

$$R_1 = \frac{Z_2 - Z_1}{Z_2 + Z_1} \tag{5}$$

$$T_{12} = \frac{2Z_2}{Z_2 + Z_1} \tag{6}$$

Similarly, the reflection coefficient R_2 and transmission coefficient T_{21} for a wave incident at the interface from Medium 2 can be written as

$$R_2 = \frac{Z_1 - Z_2}{Z_1 + Z_2} \tag{7}$$

$$T_{21} = \frac{2Z_1}{Z_1 + Z_2} \tag{8}$$

The wave propagation matrix can be formulated using following steps based on the variables shown in Fig. 9. The figure shows the interface between two different media with waves traveling along directions described by positive and negative signs. As can be seen, the total negative traveling wave in Medium 1 from the interface consists of both the reflected positive traveling incident wave from Medium 1 and the negative traveling transmitted wave from Medium 2. Hence, the electric field of the negative traveling wave in Medium 1can be written as

$$E_{1-} = R_1 E_{1+} + T_{21} E_{2-} \tag{9}$$

where the subscripts + and − represent positive and negative traveling waves, respectively. Similarly, the total positive traveling wave in Medium 2 can be expressed as

$$E_{2+} = R_2 E_{2-} + T_{12} E_{1+} \tag{10}$$

To form the required matrix, we rearrange above expressions as follows,

$$E_{1+} = \frac{1}{T_{12}} E_{2+} - \frac{R_2}{T_{12}} E_{2-} \tag{11}$$

$$E_{1-} = \frac{R_1}{T_{12}} E_{2+} + \left(T_{21} - \frac{R_1 R_2}{T_{12}} \right) E_{2-} \tag{12}$$

The reflection coefficients R_1 and R_2 are related as $R_1 = -R_2$. In addition, the transmission coefficients T_{12} and T_{21} can be substituted using $1 + R_1$ and $1 + R_2$, respectively, so that the wave propagation matrix simplifies as follows

$$\begin{bmatrix} E_{1+} \\ E_{1-} \end{bmatrix} = \frac{1}{T_{12}} \begin{bmatrix} 1 & R_1 \\ R_1 & 1 \end{bmatrix} \begin{bmatrix} E_{2+} \\ E_{2-} \end{bmatrix} \tag{13}$$

Since the wave matrix is only assumed at the location of interface, it is necessary to extend it to an arbitrary inside Medium 2 for multilayered cases. Assuming that the location of observation point is $x = x_1$ with amplitudes E'_{2+} and E'_{2-} and accounting for the phase shifts of the positive and the negative traveling waves, we can write

$$E'_{2+} = E_{2+} e^{-jkx_1} \tag{14}$$

$$E'_{2-} = E_{2-} e^{+jkx_1} \tag{15}$$

Using the electrical length $\theta_1 = kx_1$, the wave propagation matrix can be formed as

$$\begin{bmatrix} E_{2+} \\ E_{2-} \end{bmatrix} = \begin{bmatrix} e^{+j\theta_1} & 0 \\ 0 & e^{-j\theta_1} \end{bmatrix} \begin{bmatrix} E'_{2+} \\ E'_{2-} \end{bmatrix} \tag{16}$$

Substituting Eq. (16) in Eq. (13), we have

$$\begin{bmatrix} E_{1+} \\ E_{1-} \end{bmatrix} = \frac{1}{T_{12}} \begin{bmatrix} 1 & R_1 \\ R_1 & 1 \end{bmatrix} \begin{bmatrix} e^{+j\theta_1} & 0 \\ 0 & e^{-j\theta_1} \end{bmatrix} \begin{bmatrix} E'_{2+} \\ E'_{2-} \end{bmatrix} \tag{17}$$

By generalizing to an m-layered structure using the products of matrix above together with the electrical length of each layer, the generalized wave propagation matrix of the multilayered structure can be written as

$$\begin{bmatrix} E_{1+} \\ E_{1-} \end{bmatrix} = \prod_{i=1}^{m} \frac{1}{T_{i,i+1}} \begin{bmatrix} 1 & R_i \\ R_i & 1 \end{bmatrix} \begin{bmatrix} e^{+j\theta_i} & 0 \\ 0 & e^{-j\theta_i} \end{bmatrix} \begin{bmatrix} E'_{(i+1)+} \\ E'_{(i+1)-} \end{bmatrix} \tag{18}$$

3.3. Wave Propagation in Uneven FRP Interfaces

In actual delaminations as discussed previously, it is necessary to consider not only the normal incident wave cases but also waves at oblique incidence so that irregular or uneven interface structures can be analyzed. Thus, the generalized approach for an arbitrary incident angle ϕ_i is analyzed by exploring the relationship between the incident angle and the normalized intrinsic impedance [20] at each scanning location point. Thus, every measurement will be based on the reflection or transmission coefficients using the local incident angle, as shown in Fig. 10.

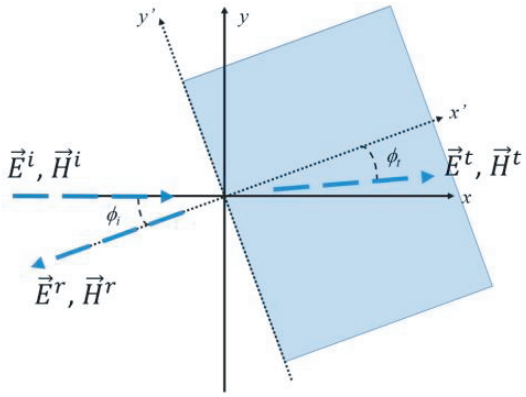

Figure 10. Wave projection scheme on dielectric slab with incident angle of ϕ_i for complex defects due to external impacts and stresses.

In this case, it is necessary to determine the critical incident angle of the incident wave due to the sensor or antenna system which limits the collection of the reflection wave from the target. In addition, calibration processes are also necessary since reflections from multiple interfaces will affect the total reflection from the test specimen.

Consider waves from air to dielectric at an incident angle of ϕ_i with the incident electric field given by

$$\vec{E}^i = \hat{z} E_0^i e^{-jk_0 x} \tag{19}$$

Coordinate transformation from (x, y, z) to (x', y', z') results in $x = x' \cos\phi_i - y' \sin\phi_i$, $y = x' \sin\phi_i + y' \cos\phi_i$, and $z = z'$. Hence, the incident wave in the new coordinate system is

$$\vec{E}^i = \hat{z}' E_0^i e^{-jk_0(x' \cos\phi_i - y' \sin\phi_i)} \tag{20}$$

The corresponding incident magnetic field is given by [20]

$$\vec{H}^i = -\hat{y} \frac{k_0}{\omega\mu_0} E_0^i e^{-jk_0 x} = -\hat{y} \frac{1}{Z_0} E_0^i e^{-jk_0 x} \tag{21}$$

where Z_0 is the intrinsic or wave impedance of air, given by $Z_0 = \sqrt{\mu_0/\varepsilon_0}$. In the new coordinate system, we can express

$$\begin{aligned} \vec{H}^i &= -\left(\hat{x}' \sin\phi_i + \hat{y}' \cos\phi_i\right) \frac{1}{Z_0} E_0^i e^{-jk_0(x' \cos\phi_i - y' \sin\phi_i)} \\ &= -\hat{x}' \sin\phi_i \frac{1}{Z_0} E_0^i e^{-jk_0(x' \cos\phi_i - y' \sin\phi_i)} - \hat{y}' \cos\phi_i \frac{1}{Z_0} E_0^i e^{-jk_0(x' \cos\phi_i - y' \sin\phi_i)} \end{aligned} \tag{22}$$

The effective intrinsic impedance of Medium 1, Z_1, can be obtained by relating the corresponding components of incident electric and magnetic fields, namely

$$E_{z'}^i = E_0^i e^{-jk_0(x' \cos\phi_i - y' \sin\phi_i)} \tag{23}$$

$$H_{y'}^i = -\cos\phi_i \frac{1}{Z_0} E_0^i e^{-jk_0(x' \cos\phi_i - y' \sin\phi_i)} \tag{24}$$

from which we have

$$Z_1 = \frac{-E^i_{z'}}{H^i_{y'}} = Z_0 \sec\phi_i \tag{25}$$

Similarly, the transmitted E-field and H-field at a transmitted angle of ϕ_t are given by

$$\vec{E}^t = \hat{z}' E^t_0 e^{-jk(x'\cos\phi_t - y'\sin\phi_t)} \tag{26}$$

$$\vec{H}^t = -\hat{x}'\sin\phi_t \frac{1}{Z_d} E^t_0 e^{-jk(x'\cos\phi_t - y'\sin\phi_t)} - \hat{y}'\cos\phi_t \frac{1}{Z_d} E^t_0 e^{-jk(x'\cos\phi_t - y'\sin\phi_t)} \tag{27}$$

where $Z_d = Z_0/\sqrt{(\varepsilon_r + \frac{\sigma}{j\omega\varepsilon_0})}$ is the intrinsic impedance of dielectric region (Medium 2). Thus, the effective intrinsic impedance in Medium 2, Z_2, can be expressed using the components of transmitted electric and magnetic field as

$$E^t_{z'} = E^t_0 e^{-jk(x'\cos\phi_t - y'\sin\phi_t)} \tag{28}$$

$$H^t_{y'} = -\cos\phi_t \frac{1}{Z_d} E^t_0 e^{-jk(x'\cos\phi_t - y'\sin\phi_t)} \tag{29}$$

$$Z_2 = \frac{-E^t_{z'}}{H^t_{y'}} = Z_d \sec\phi_t \tag{30}$$

Here, the effective intrinsic impedance can be normalized so that it can be applied to any dielectric layer with known electrical properties. If the wave travels in same region (Medium 1) the effective intrinsic impedance can be normalized as 1. In case of wave traveling from Medium 1 (air) to Medium 2 (dielectric), the normalized effective intrinsic impedance can be expressed as

$$Z = \frac{Z_2}{Z_1} = \frac{Z_d \sec\phi_t}{Z_0 \sec\phi_i} = \frac{\cos\phi_i}{\sqrt{\varepsilon_r + \frac{\sigma}{j\omega\varepsilon_0}}\cos\phi_t} \tag{31}$$

Snell's law can be now applied based on the relationship $k_o \sin\phi_i = k\sin\phi_t$ to remove the dependence on ϕ_t. This yields

$$Z = \frac{\cos\phi_i}{\sqrt{\varepsilon_r + \frac{\sigma}{j\omega\varepsilon_0} - \sin^2\phi_i}} \tag{32}$$

which is only in terms of the incident angle at the interfaces. Thus, the normalized effective impedance can be applied to the wave propagation matrix to analyze the wave propagation through multilayered structures with uneven interfaces due to external forces and impacts.

4. MICROWAVE IMAGING SCHEME FOR APPLICATIONS

4.1. Formulation of Scattering from Dielectric Interfaces

For the transmitted noiselet waveform, the z-directed electric field amplitudes have constant non-zero random values at N discrete frequencies over the UWB operating range, given by

$$\vec{E}^i = \hat{z}\cdot\left[E_1 e^{-jk_1 x} + E_2 e^{-jk_2 x} + \ldots + E_N e^{-jk_N x}\right] = \hat{z}\cdot\sum_{i=1}^{N} E_i e^{-jk_i x} \tag{33}$$

where E_i is the amplitude of electrical field of noiselet waveform, and E_i and k_i are the amplitudes and wavenumbers at each discrete frequency. While the overall noiselet waveform is formed as the sum of individual frequency components, the analysis is simplified by considering each frequency separately and them summing the responses later via superposition.

Consider the incident wave at the i-th frequency component traveling along the $+x$-direction whose amplitude is expressed as $E^i = E_i e^{-jk_i r}$ at a standoff distance r from the antenna to the first surface. We use the theory of small reflections from each interface, which approximates the interface transmission

coefficients to unity and neglects multiple reflections within layers. The total reflection coefficient from an m-layered dielectric material with layer thicknesses $d_1, d_2, \ldots, d_m$ and corresponding wavenumbers $k_{1(i)}, k_{2(i)}, \ldots, k_{m(i)}$ can be expressed as [19]

$$\Gamma_{\text{total}} \cong \Gamma_0 + \Gamma_1 e^{-j2k_{1(i)}d_1} + \Gamma_2 e^{-j2\left(k_{1(i)}d_1 + k_{2(i)}d_2\right)} + \ldots + \Gamma_m e^{-j2\left(k_{1(i)}d_1 + k_{2(i)}d_2 + \ldots + k_{m(i)}d_m\right)} \tag{34}$$

where Γ_j is the interface reflection coefficient between the $(j-1)$-th and j-th layers.

4.2. Scattering Scheme from Uneven Curved Interfaces

As we discussed earlier, multilayered dielectric composite materials can deform due to internal and external factors such as humidity, inner delaminations, and stress. Such deformations cause uneven areas on both surfaces and interfaces. Fig. 11 shows an example of a dielectric layer with an uneven surface.

The actual range from the sensor to uneven surface is not constant and varies due to the swollen or dented area. The distance from the antenna to any scanning point can be expressed as

$$x(n) = r - y(n)\tan\phi_i(n) \tag{35}$$

where r is the standoff distance between the sensor and the "flat" surface; $y(n)$ is the n-th measurement point; $\phi_i(n)$ is the local incident angle at n-th data point. This actual distance $x(n)$ must be used in the imaging algorithms discussed later. The reflection and transmission coefficients are also dependent on the local incident angles and normalized impedances, and the correct expressions must be used for accurate computations from uneven dielectric interfaces.

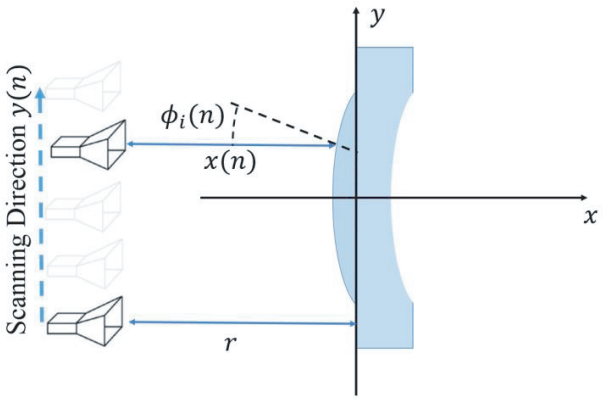

Figure 11. Uneven dielectric surface schematic to determine the scattering from the target specimen.

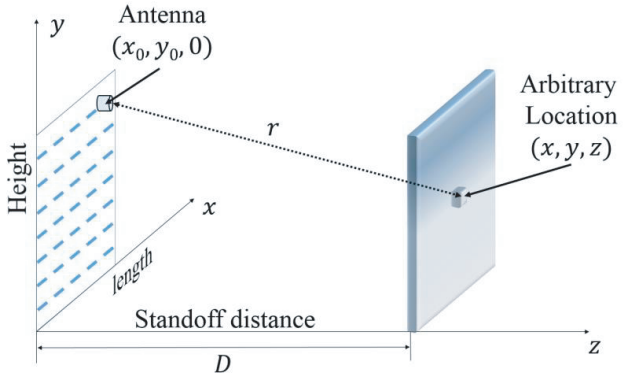

Figure 12. Synthetic aperture radar scanning measurement scheme for microwave imaging.

4.3. Synthetic Aperture Radar Scanning Algorithm for Image Reconstruction

Figure 12 shows the schematic view of data acquisition for microwave imaging using raster scanning over the target specimen, where (x, y, z) represents the location of an arbitrary point scatterer within the 3D target. The aperture plane is located at $z = 0$ and thus, the antenna location is $(x_0, y_0, 0)$. The standoff distance to the front face of the target is D. The sensor is considered to be operating in the quasi-monostatic mode. The radar antenna begins scanning for echo data collection starting at the one end of the x-axis, parallel to the length direction of target specimen, and acquires the range profile at the sampling intervals. After the range data acquisition is completed at various steps on the x-grid, the radar reproduces a 2D data matrix for xy-domain in the form of in-phase (I) and quadrature (Q) components. The radar, then, moves to the next location in the y-direction and acquires another range profile data. This process is repeated for every interval step.

In SAR processing, there are several techniques that may be applied for optimization and calibration of image processing, such as the range doppler algorithm (RDA), chirp scaling algorithm (CSA), range migration algorithm (RMA) [21, 22]. Each algorithm has its strengths and weaknesses based on the waveforms and testing conditions under which it is being conducted. Since SAR scanning in our application is performed in the near-field range and test specimens are assumed as static targets, data calibration is necessary. The near-field wavefront has a curvature or parabolic shape by nature, and thus, the received reflected wavefront will have the opposite curvature compared to the original wavefront. Thus, the RMA is the best choice for the near-field radar system to calibrate the acquired data. The block diagram of the RMA procedure is shown in Fig. 13.

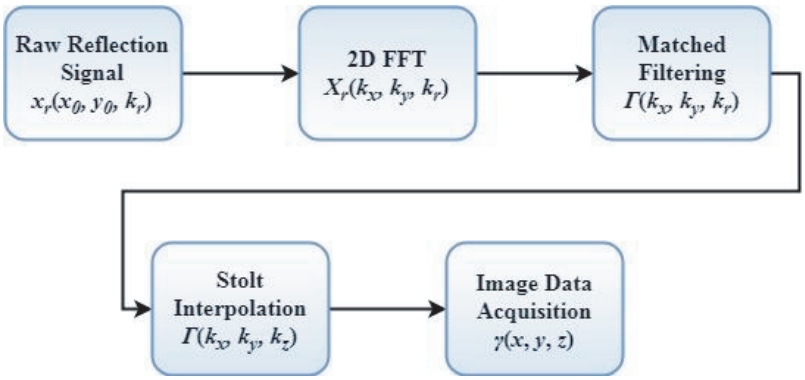

Figure 13. Block diagram of range migration algorithm process for near-field SAR scanning system.

The advantage of RMA is the process called Stolt interpolation [23] which relocates near-field received data into a plane wave. Stolt interpolation was originally introduced in geology for processing seismic data. Since wavefronts for seismic data collection are similar to near-field SAR techniques, Stolt interpolation is applicable for optimization and calibration of received raw data.

The theoretical expansion of RMA will be described using the three dimensional coordinate references from Fig. 12, following the development in [24]. Scanning data are acquired point-by-point, following which a data matrix is formed for image reconstruction after acquiring data from all the scanning or data points. Assume that the noiselet waveform $x_t(f)$ is transmitted from a typical sensor location $(x_0, y_0, 0)$ at an instantaneous frequency f. The sensor synthesizes a two-dimensional antenna aperture located on the xy-plane. The spacing between each scanning point, Δx_0 and Δy_0 in the x- and y-directions respectively, satisfies the Nyquist sampling criterion to avoid aliasing effects, i.e., the typical spacing value is approximately half the wavelength at the highest operating frequency. At each point, data are collected over the operating frequency bandwidth Δf; thus, acquired backscattered signals will contain information on spatial location and phase information based on the operating frequency. Denoting the reflection coefficient as $\gamma(x, y, z)$ at any arbitrary location of target specimen, the measured backscattered signal at $(x_0, y_0, 0)$ can be written as

$$(x_0, y_0, 0) \approx \gamma(x, y, z) \cdot e^{-jk_r z} \cdot e^{-jk_r r} \tag{36}$$

where $r = \sqrt{(x - x_0)^2 + (y - y_0)^2 + z^2}$, $k_r = 2\pi f/c$ is the spatial wavenumber in air corresponding to the operating frequency, and c is the speed of light.

Although part of the wave propagation is in the medium (when $z > D$), we use only the wavenumber in air, since we assume that $|z - D| \ll \lambda$, i.e., that the total thickness of the sample target is much less than the wavelength. This is the reason for the approximate sign in Equation (36).

The 3D reflectivity function for a distributed target can be obtained as

$$\gamma(x, y, z) = \int_{k_r} \int_{y_0} \int_{x_0} x_r(x_0, y_0, 0) \cdot e^{jk_r z} \cdot e^{jk_r \sqrt{(x-x_0)^2 + (y-y_0)^2 + z^2}} dx_0 dy_0 dk_r \tag{37}$$

which can be recast as [24]

$$\gamma(x,y,z) = \int_{k_r} e^{jk_r z} \left[\int_{y_0} \int_{x_0} x_r(x_0,y_0,0) \cdot e^{jk_r\sqrt{(x-x_0)^2+(y-y_0)^2+z^2}} dx_0 dy_0 \right] dk_r \tag{38}$$

Equations (37) and (38) can be recognized as solutions to the linear inversion scattering formulation. A 2D weighting function is applied prior to focusing to force the backscattered fields to vanish at the aperture boundaries.

We assume that the following 2D spatial Fourier Transform in the x- and y-directions, given by [24]

$$E(k_x,k_y) = \iint e^{jk_r\sqrt{(x-x_0)^2+(y-y_0)^2+z^2}} \cdot e^{-j(k_x x+k_y y)} dxdy \tag{39}$$

is known. This permits the evaluation of the 2D convolution in the aperture coordinates (x_0, y_0) as a complex product in the Fourier domain. Using the method of stationary phase outlined in [24], we obtain

$$E(k_x,k_y) \cong \frac{-j2\pi k_r}{k_z^2} \cdot e^{jk_z z} \tag{40}$$

where $k_z = \sqrt{k_r^2 - k_x^2 - k_y^2}$. The 3D reflectivity image is then given by

$$\gamma(x,y,z) \cong \int_{k_x} \int_{k_y} \int_{k_r} X_r(k_x,k_y,k_r) \cdot \left(-\frac{j2\pi k_r}{k_z^2}\right) \cdot e^{j(k_x x+k_y y+k_z z)} dk_x dk_y dk_r \tag{41}$$

where $X_r(k_x, k_y, k_r)$ is the Fourier transform of the backscattered signals. Since the wavenumber domain backscattered data are to be resampled uniformly in k_z prior to performing the 3D inverse Fourier Transform in Equation (41), we substitute $k_r \to k_z$. Then, we obtain

$$\gamma(x,y,z) \cong \int_{k_x} \int_{k_y} \int_{k_z} X_r(k_x,k_y,k_z) \cdot \left(\frac{-j2\pi}{k_z}\right) \cdot e^{j(k_x x+k_y y+k_z z)} dk_x dk_y dk_z \tag{42}$$

which can form the data matrix $s_{\text{image}}(x, y, z)$ for the 3D image reconstruction of the target specimen. The following shows an example 2D image matrix of size $m \times n$ data points at the $z = z'$ plane:

$$s_{\text{image}}(x,y,z') = \begin{bmatrix} \gamma(x_1,y_1,z') & \gamma(x_2,y_1,z') & \cdots & \gamma(x_m,y_1,z') \\ \gamma(x_1,y_2,z') & \gamma(x_2,y_2,z') & \cdots & \gamma(x_m,y_2,z') \\ \vdots & \vdots & \ddots & \vdots \\ \gamma(x_1,y_n,z') & \gamma(x_2,y_n,z') & \cdots & \gamma(x_m,y_n,z') \end{bmatrix} \tag{43}$$

Similarly, 2D images can be obtained at other orthogonal planes given by $x = x'$ or $y = y'$ by simply taking the appropriate data matrix collected at that desired location.

4.4. Applications of Quasi-3D Imaging on Nondestructive Testing and Evaluations

As discussed earlier, the FRP composites are formed as laminated and sandwiched structures using woven fiber sheets or slabs; thus, interlaminar or intralaminar delamination scan occur during manufacture or usage. Microwave imaging using SAR scanning for NDT&E is a promising technique to map the internal defects of FRP composites. Structural schematics with delamination and defect will be provided with reconstructed image results.

Figure 14 shows the generalized mechanism of image reconstruction on the target specimen using the data matrix acquired during the SAR scanning algorithm. Two dielectric layers ($\varepsilon_r = 4.0$) with thickness of 5 cm within a 5-cm air gap between them ($\varepsilon_r = 1.0$) are considered to demonstrate the data matrix implementation and the final reconstructed images. Further simulations use actual values for the FRP material.

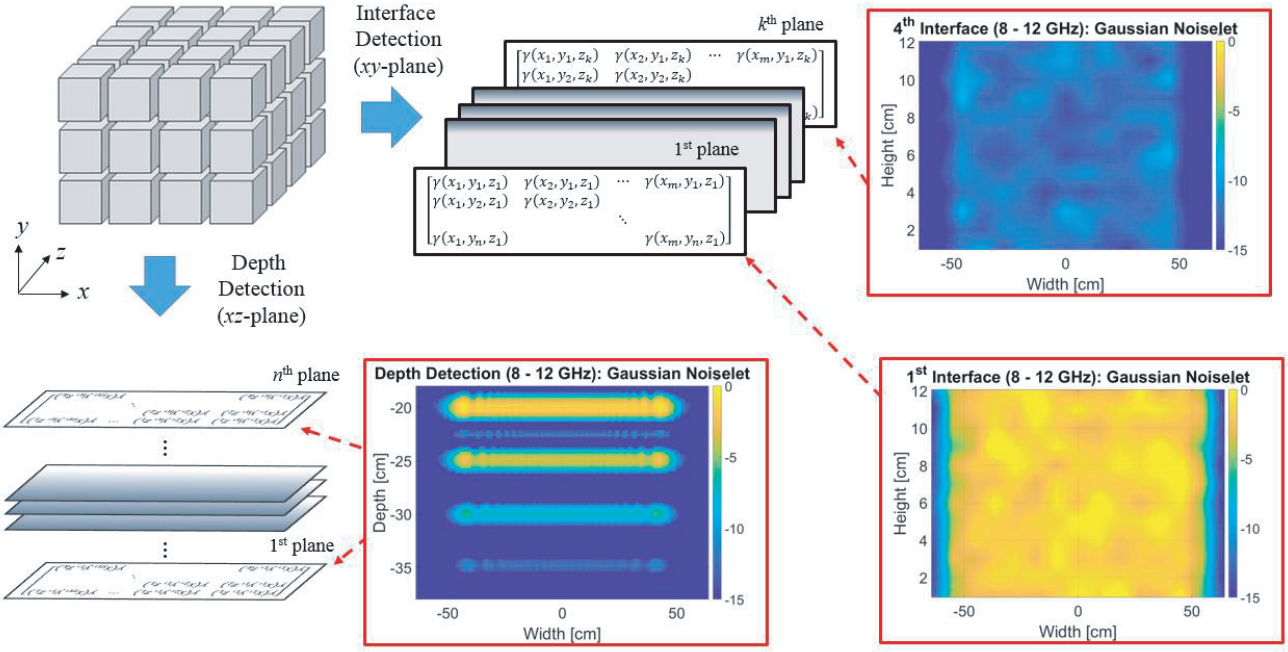

Figure 14. Three dimensional overview of data matrix acquisition for image reconstruction of xy-plane (defect on interfaces) and xz-plane (depth of interfaces) with SAR scanning scheme.

The range or depth resolution, which will determine the potential of interface detection, can be determined by the bandwidth of the transmit signal frequency as well as the dielectric constant of the material. Due to the layer depths of FRP composites, it is very important to determine the suitable resolution of detection for obtaining proper characterization of interfaces. Since these defects are internal to the structure and are relatively small in size, the radar signals operating over the appropriate frequency range ensures signal penetration within the structure, which can then be exploited to detect these defects as anomalies. The depth resolution is given by

$$\Delta R = \frac{c}{2\Delta f\sqrt{\varepsilon'_r}} \tag{44}$$

where c is the speed of light, and Δf is the bandwidth [9]. Theoretically, it is beneficial to choose a wider bandwidth to achieve better depth resolution. In practice, however, there are restrictions on frequency band choices due to system limitations.

The penetration depth within the medium is given by [20]

$$\delta_p = \frac{c}{2\pi f\sqrt{\varepsilon'_r}}\left[\frac{2}{\sqrt{1+\tan^2\delta}-1}\right]^{1/2} \tag{45}$$

where $\tan\delta$ is the loss tangent given by $\varepsilon''_r/\varepsilon'_r$. The penetration depth is a critical factor for the depth detection limits. Thus, it is necessary to choose the optimal frequency band by exploring the tradeoffs between depth resolution and penetration depth. Based upon our application and limits of system availability, the X-band (8–12 GHz) frequency range is expected to achieve the desired resolution and good penetration with relatively lower loss for high-resolution probing of defects in laminated FRP structures.

In order to perform microwave imaging analysis, it is necessary to assume appropriate dielectric properties for the FRP composite material. Data from a few references are shown in Table 1 [25–27]. The variations are due to the actual composition of the composite and properties such as density, fiber diameter, fiber orientation, etc.

Table 1. Dielectric constant data on typical FRP composites at X-band.

Material	Frequency (GHz)	Real part (ε'_r)	Imaginary part (ε''_r)	Reference
E-glass	8.0–11.0	4.54–5.24	0.3–1.12	[25]
E-glass	8.2–12.4	4.95–5.03	0.12–0.24	[26]
Fiberglass	8.2–12.4	3.30–3.40	0.07–0.15	[27]

Based on the data presented in Table 1, we assume $\varepsilon'_r = 5$ and $\varepsilon''_r = 0.4$ as typical values of the dielectric constant for the FRP material. The computed depth resolution and penetration depth using our assumed values are computed as 1.68 cm and 5.34 cm, respectively.

Figures 15 to 19 provide SAR NDT&E images on FRP plates having dimensions of 100 cm in width (x-axis), 12 cm in height (y-axis), and 5 cm in thickness (z-axis). The standoff distance D is assumed to be 20 cm. Quasi-3D images are obtained by stacking down-range images from specific inspection depths. Several conditions of delamination layers and structures, due to internal and external factors discussed earlier, are investigated to provide various scenarios.

Before continuing, several assumptions are made for the microwave analysis on FRP composites. As is already known that FRP composites in general are laminated and sandwiched by stacking fiber sheets or plates with epoxy materials. Since the epoxy layers are very thin, their dielectric properties can be neglected, and the FRP structure can be considered as a single dielectric layer with no delamination present between the woven fiber layers. Thus, the only delamination layers (consisting of air gaps) will be considered for the multilayer analysis and corresponding quasi-3D imaging results will be provided in the following figures.

Figure 15 provides the reconstructed images of a perfect FRP sample without any defect from a manufacturing process. Quasi-3D images of interface detection on Fig. 15 are collected by taking data steps of 1.0 cm on the z-axis. As can be seen, reflections from two interfaces, between air to FRP and FRP to air, are mapped and reconstructed to form both depth and interface detection images. One

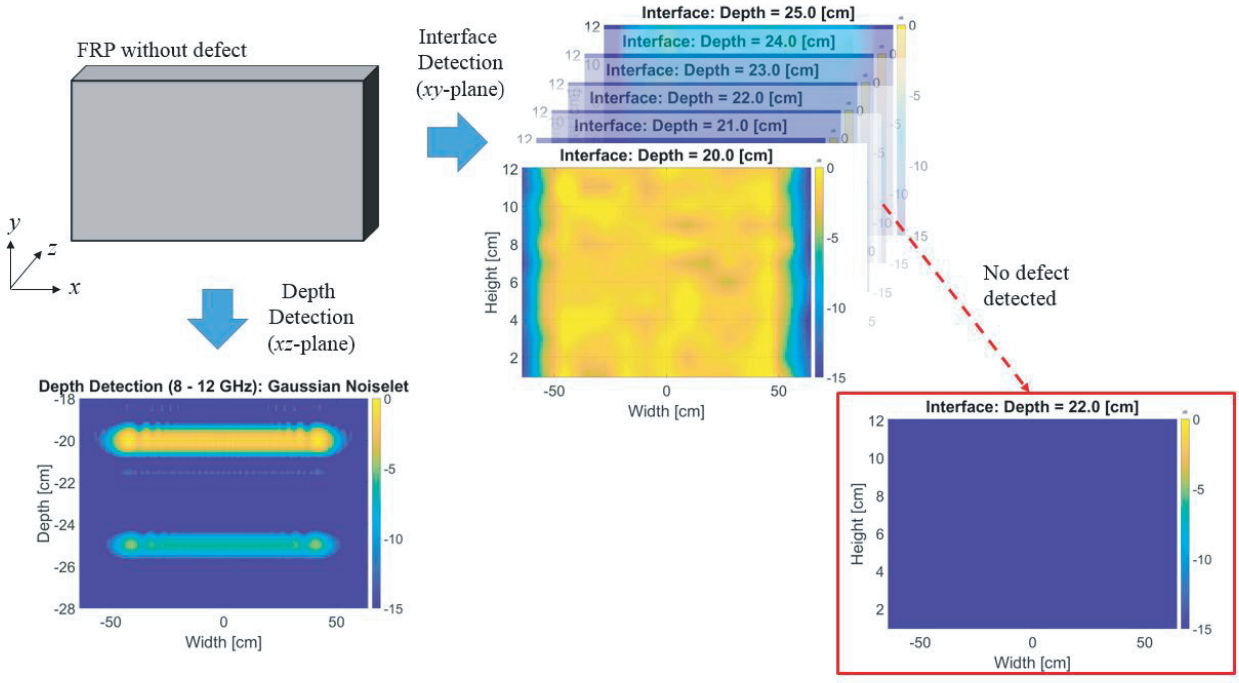

Figure 15. Quasi-3D image reconstruction for FRP layer without delamination present.

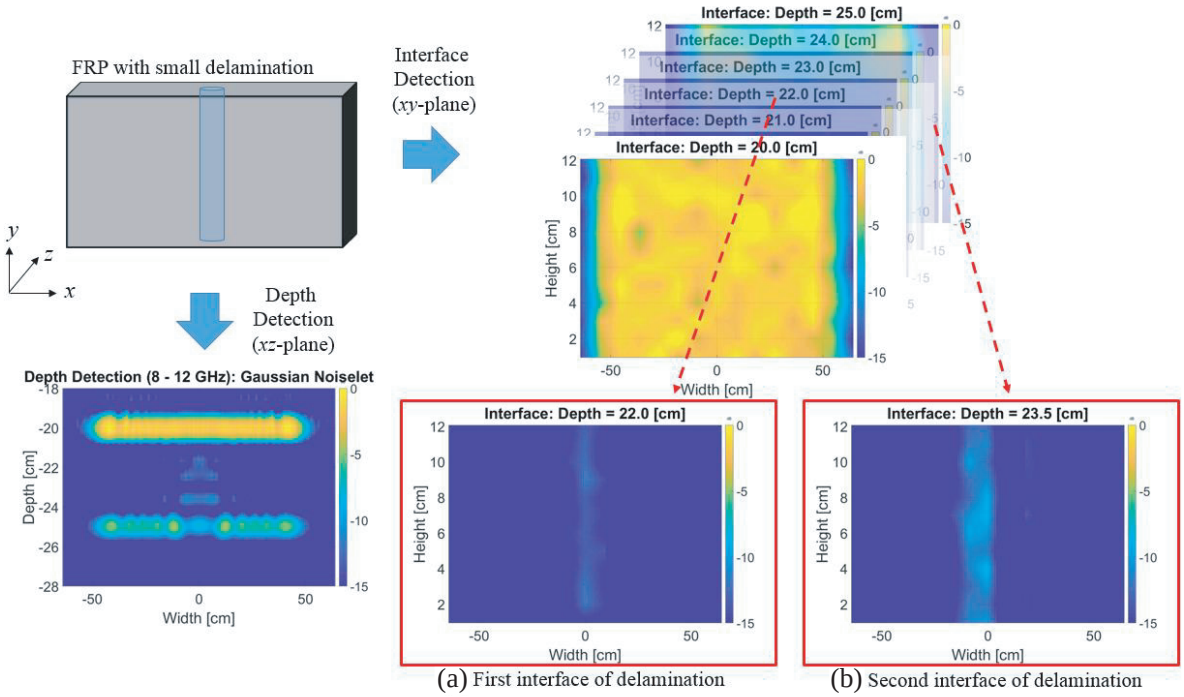

Figure 16. Quasi-3D image reconstruction for FRP layer. A 5-cm wide delamination layer is located at 2-cm depth from the surface and its thickness is assumed to be 1.5 cm.

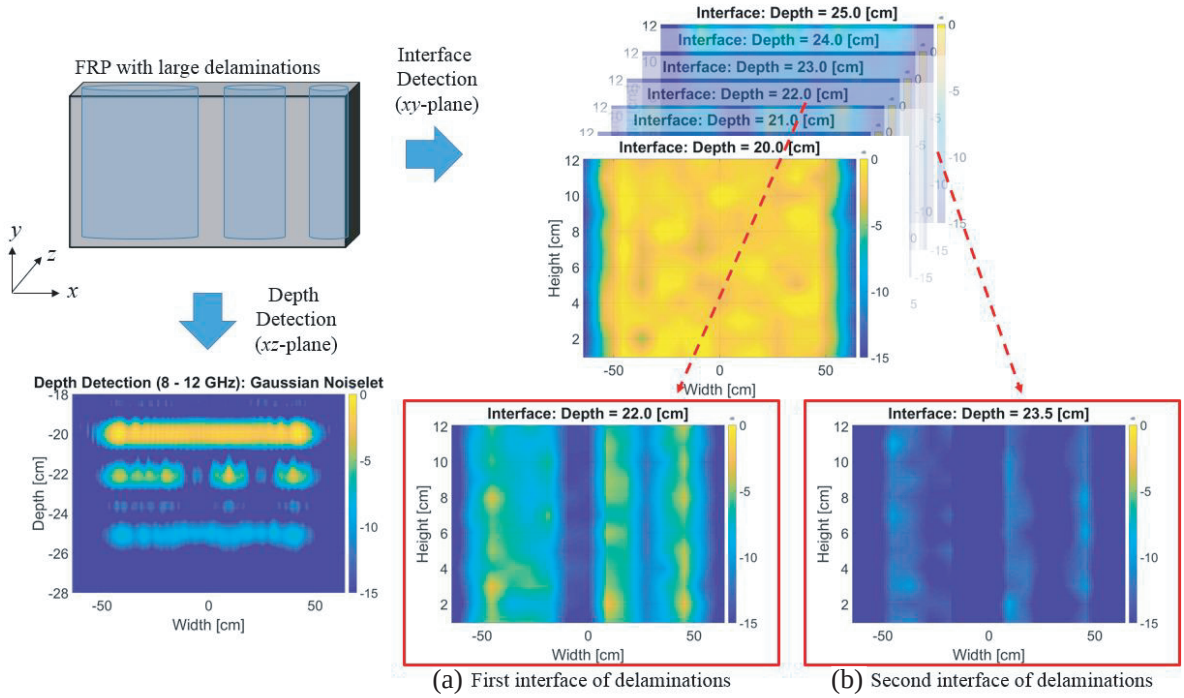

Figure 17. Quasi-3D image reconstruction for FRP layer with multiple delaminations. Wider delamination layers are assumed as expected to increase from initial small delaminations during service life due to external factors. Delamination layers are located approximately at 2-cm depth from the surface and their thicknesses are assumed to be 1.5 cm.

sample image of interface detection is also enlarged to inform that no reflection appears during the wave propagation through the FRP composite layer without delaminations.

Delamination layers are then introduced within the FRP composites in different structural configurations. In these approaches, two types of FRPs are assumed: flat plate case, and bent structure case.

Figures 16 and 17 are designed FRP plates with perfectly flattened interfaces with delaminations, while Figs. 18 and 19 are based on bent FRPs assuming that external factors caused the gentle curved interfaces. In case of Figs. 16 and 18, it is assumed that a small delamination is initially produced during the manufacturing procedure. On the other hand, Figs. 17 and 19 show situations after a certain service life which may induce delamination growth due to stress and impact. Each delamination layer is assumed to be located at a depth of 2.0 cm under the front surface and having a thickness of 1.5 cm at the largest gap. Delaminations are also assumed to have uneven interfaces with gradual curves based on the structural configurations investigated.

Quasi-3D images shown in Fig. 16 are able to locate and size small delaminations. Compared to the second interface reflection, the image dimension from the first interface at the delamination layer is weaker, but nevertheless detectable. Furthermore, as shown in Fig. 17, multiple delaminations with larger widths due to service can also be imaged very well. As expected, delamination layers under flat FRP assumption provide relatively accurate information on both widths and depth locations and show denser reflections from the first interface of delaminations as their width increases.

Since the detection of flat FRP composites shows relatively accurate results, it is worthwhile to apply the approach to a more complex structure, i.e., a bent FRP structure with similar assumption from a small initial delamination (Fig. 18) to large delaminations (Fig. 19) occurring during its service. From Fig. 18, we note that the first interface of the small curved delamination layer can be imaged, although the reflection from second interface (back) is hardly detected. The delamination layer is also formed as a gentle curved interface; thus, the reflection from back interface of delamination might be harder to detect compared to the reflections from other interfaces.

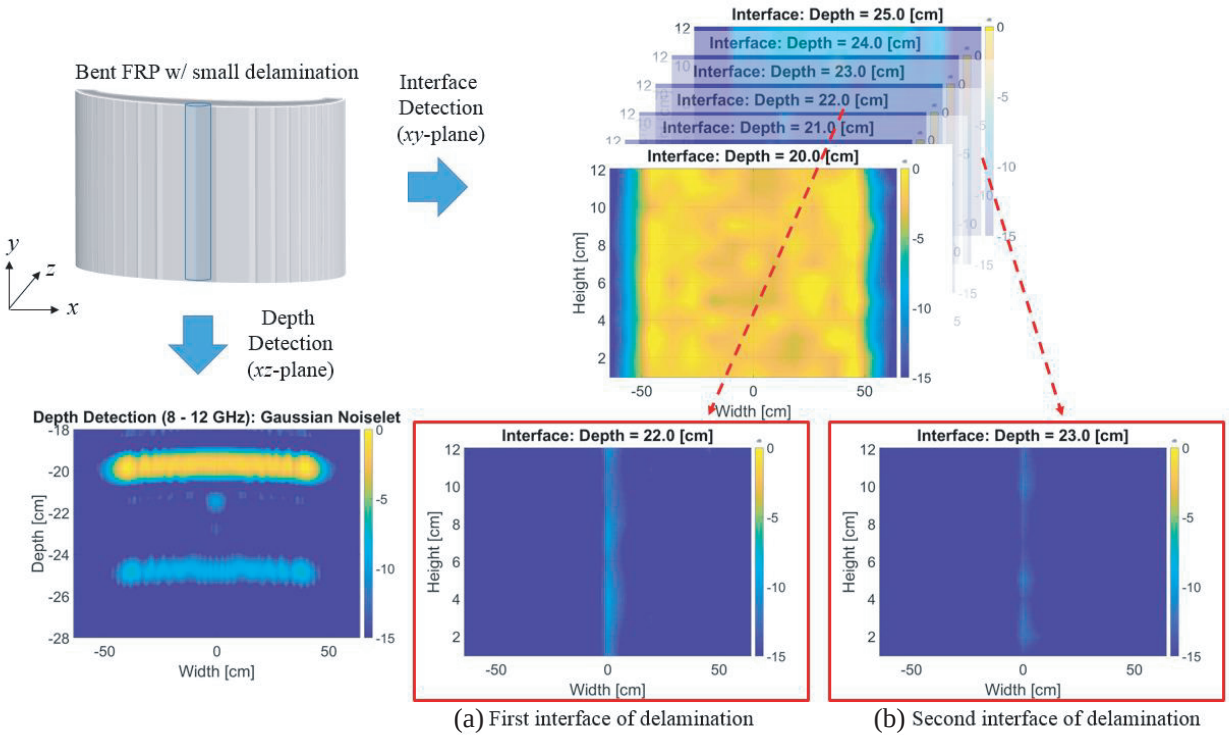

Figure 18. Quasi-3D image reconstruction for uneven FRP (swelled up 0.5 cm at the center) with small delamination presents. Delamination layer is located approximately at 2.0-cm depth from the surface and the thickness of layers are assumed to be 1.5 cm.

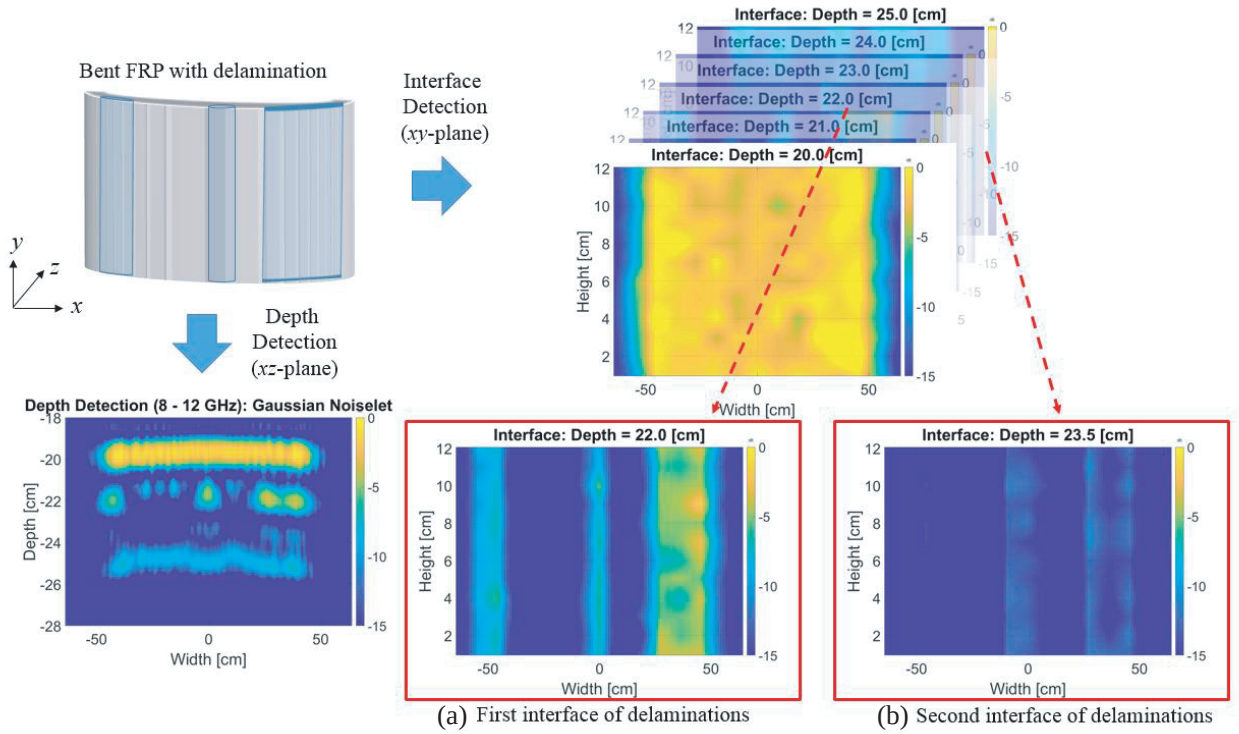

Figure 19. Quasi-3D image reconstruction for uneven FRP with multiple delaminations. Wider delamination layers are assumed as expected to increase from initial small delaminations during service life due to external factors. Delamination layers are located approximately at 2.0-cm depth from the surface and their thicknesses are assumed to be 1.5 cm.

Figure 19 provides inaccurate information on depth detection at the second interfaces of delaminations due to the complex computational steps involved in calibration based on each measurement point. Yet, interface detection images provide relatively accurate widths of delamination layers which can still be applicable for defect detection systems for NDT&E. Moreover, additional calibrations and optimizations on the computational processes could improve results in advance if higher accuracy in depth detection is necessary. Accurate delamination extent estimation may not be necessary since the purpose of monitoring is to determine the service life of the structure by revealing the presence of delaminations.

5. CONCLUSIONS

In this paper, the ultrawideband (UWB) radio frequency (RF) noiselet waveform is introduced with theoretical backgrounds and its optimization based on maximizing the peak-to-sidelobe ratio is provided. UWB noiselet is then applied to microwave imaging which is useful for nondestructive testing and evaluation. Synthetic aperture radar scanning technique, in specific, is considered for data acquisition from multilayered fiber reinforced plastic (FRP) composites of different shapes with various dimensions of delamination layers. The algorithm for image reconstruction is also discussed in detail for near-field system calibration due to the shape of transmitted wavefront and the location of the reflection wave inaccuracy. From a structural point of view, the approach using generalized incident waves is developed to analyze not only flat surfaces, but also uneven interfaces as wave travels through the dielectric media. Moreover, quasi-3D images of interfaces (xy-plane) are acquired by gathering and organizing 2D image matrix using the dataset from depth profiles (z-axis), which can be determined by analyzing depth detection data matrix and reconstructed images. Thus, the structural diagnosis of dielectric materials, including FRPs, is made more convenient and powerful by quasi-3D image acquisition using UWB RF

noiselets. The novelty in our approach presented herein are the optimization of the noiselet waveform for best sidelobe performance as well as the application of quasi 3D imaging towards realistic damaged structures.

While our approach using an optimized noiselet waveform of 4-GHz bandwidth can detect defects of the order of ~ 1.5 cm, better resolutions can be achieved by employing super-resolution techniques. The resolution offered by the conventional Fast Fourier Transform-based (FFT-based) spectrum estimation techniques is strictly limited by the transmitted bandwidth. Hence, very wide bandwidth might be needed to satisfy typical range resolution requirements in many applications involving multilayered structures. However, transmitting very wide band microwave signals might be prohibitive in practice.

One such technique is the well-known multiple signal classification (MUSIC) algorithm [28], which is widely used in communications, radar, and antenna beamforming, and which has shown to offer higher spectral resolution compared to the conventional FFT-based techniques. The strength of MUSIC is not simply in the ease of its mathematical formulation and implementation, but also in its foundation, which is based on the physical principles of the scattering phenomenon. Examples of the application of the MUSIC technique to NDT are described herein.

Super-resolution is very important for the signal processing of ground penetration radar to resolve closely buried targets. The MUSIC algorithm has been successfully implemented for signal and image processing for GPR applications [29]. By performing singular value decomposition of the multistatic response matrix from a dipole array illuminating a half-space containing an inclusion, MUSIC processing provided a cost functional whose magnitude peaked at the inclusion center [30]. The MUSIC algorithm was also investigated to locate small dielectric cylinders of specific characteristics in noise-free and noisy scenarios [31]. The detection capability and the resolution offered by the MUSIC algorithm was seen to outperform the FFT-based algorithm when used to process wideband frequency-modulated continuous-wave (FMCW) radar returns, particularly for the purpose of evaluating single and layered dielectric structures [32]. New formulations have been investigated to solve the inverse scattering problem for locating isolated inclusions within a homogeneous noise-free and noisy biaxial anisotropic permeable background using the MUSIC algorithm [33]. We therefore believe that the application of the MUSIC algorithm will improve the resolution using our optimized noiselet waveforms.

ACKNOWLEDGMENT

This work was supported by the US Office of Naval Research Contract Number N00014-15-1-2021 (POC: William Nickerson).

REFERENCES

1. Narayanan, R. M., "Through-wall radar imaging using UWB noise waveforms," *J. Franklin Inst.*, Vol. 345, No. 6, 659–678, 2008.
2. Kulpa, K., K. Lukin, W. Miceli, and T. Thayaparan, "Signal processing in noise radar technology," *IET Radar Sonar Navig.*, Vol. 2, No. 4, 229–232, 2008.
3. Dawood, M. and R. M. Narayanan, "Multipath and ground clutter analysis for a UWB noise radar," *IEEE Trans. Aerosp. Electron. Syst.*, Vol. 38, No. 3, 838–853, 2002.
4. Chen, P. H., M. C. Shastry, C. P. Lai, and R. M. Narayanan, "A portable real-time digital noise radar system for through-the-wall imaging," *IEEE Trans. Geosci. Remote Sens.*, Vol. 50, No. 10, 4123–4134, 2012.
5. Tarchi, D., K. Lukin, J. Fortuny-Guasch, A. Mogyla, P. Vyplavin, and A. Sieber, "SAR imaging with noise radar," *IEEE Trans. Aerosp. Electron. Syst.*, Vol. 46, No. 3, 1214–1225, 2010.
6. Kim, T. H. and R. M. Narayanan, "Wideband radio frequency noiselet waveforms for multiresolution nondestructive testing of multilayered structures," *Progress In Electromagnetics Research B*, Vol. 81, 1–23, 2018.
7. Coifman, R., F. Geshwind, and Y. Meyer, "Noiselets," *Appl. Comput. Harmon. Anal.*, Vol. 10, No. 1, 27–44, 2001.

8. Candes, E. and J. Romberg, "Sparsity and incoherence in compressive sampling," *Inverse Prob.*, Vol. 23, 969–985, 2007.
9. Keep, D. N., "Frequency-modulation radar for use in the mercantile marine," *Proc. IEE — Part B: Radio Electr. Electron.*, Vol. 103, No. 10, 519–523, 1956.
10. Narayanan, R. M., X. Xu, and J. A. Henning, "Radar penetration imaging using ultra-wideband (UWB) random noise waveforms," *IET Radar Sonar Navig.*, Vol. 151, No. 3, 143–148, 2004.
11. Sivadas, N. A. and S. S. Mohammed, "A joint technique for sidelobe suppression and peak-to-average power ratio reduction in non-contiguous OFDM-based cognitive radio networks," *Int. J. Electron.*, Vol. 104, No. 2, 190–203, 2017.
12. Navagato, M. D. and R. M. Narayanan, "Microwave imaging using ultra-wideband noise waveforms for nondestructive testing of multilayer structures," *Proc. SPIE Conf. on Radar Sensor Technology XXII*, 1063314-1–1063314-13, Orlando, FL, USA, Apr. 2018.
13. Bossi, R. H. and G. E. Georgeson, "Nondestructive testing of composites," *Mater. Eval.*, Vol. 76, No. 8, 1049–1060, 2018.
14. Sato, N., M. Hojo, and M. Nishikawa, "Intralaminar fatigue crack growth properties of conventional and interlayer toughened CFRP laminate under mode I loading," *Composites Part A*, Vol. 68, 202–211, 2015.
15. Agarwal, B. D. and L. J. Broutman, *Analysis and Performance of Fiber Composites*, John Wiley & Sons, New York, NY, USA, 1990.
16. Garrett, K. W. and J. E. Bailey, "Multiple transverse fracture in 90° cross-ply laminates of a glass fiber-reinforced polyester," *J. Mater. Sci.*, Vol. 12, No. 1, 157–168, 1977.
17. Karandikar, P. and T.-W. Chou, "Characterization and modeling of microcracking and elastic-moduli changes in Nicalon CAS composites," *Compos. Sci. Technol.*, Vol. 46, No. 3, 253–263, 1993.
18. Zhong, Y. and S. C. Joshi, "Initiation of structural defects in carbon fiber reinforced polymer composites under hygrothermal environments," *J. Compos. Mater.*, Vol. 50, No. 8, 1085–1097, 2016.
19. Narayanan, R. M. and R. James, "Microwave nondestructive testing of galvanic corrosion and impact damage in carbon fiber reinforced polymer composites," *Int. J. Microwaves Appl.*, Vol. 7, No. 1, 1–15, 2018.
20. Balanis, C. A., *Advanced Engineering Electromagnetics*, 2nd Edition, John Wiley & Sons, New York, NY, USA, 2012.
21. Richards, M. A., *Fundamentals of Radar Signal Processing*, McGraw-Hill, New York, NY, USA, 2005.
22. Dehmollaian, M. and K. Sarabandi, "Refocusing through building walls using synthetic aperture radar," *IEEE Trans. Geosci. Remote Sens.*, Vol. 46, No. 6, 1589–1599, Jun. 2008.
23. Stolt, R. H., "Migration by Fourier transform," *Geophys.*, Vol. 43, No. 1, 23–48, 1978.
24. Lopez-Sanchez, J. M. and J. Fortuny-Guasch, "3-D radar imaging using range migration techniques," *IEEE Trans. Antennas Propag.*, Vol. 48, No. 5, 728–737, 2000.
25. Zoughi, R. and B. Zonnefeld, "Permittivity characteristics of kevlar, carbon composites, E-glass, and rubber (33% carbon) at X-band (8–12 GHz)," *Review of Progress in Quantitative Nondestructive Evaluation*, Vol. 10B, Chapter 38, 1431–1436, Plenum Press, New York, NY, USA, 1991.
26. Seo, I. L., W. S. Chin, and D. G. Lee, "Characterization of electromagnetic properties of polymeric composite materials with free space method," *Compos. Struct.*, Vol. 66, 533–542, 2004.
27. Tereshchenko, O. V., F. J. K. Buesink, and F. B. J. Leferink, "Measurement of complex permittivity of composite materials using waveguide method," *Proc. 10th International Symp. on Electromagnetic Compatibility (EMC Europe 2011)*, 52–56, York, UK, Sep. 2011.
28. Schmidt, R. O., "Multiple emitter location and signal parameter estimation," *IEEE Trans. Antennas Propag.*, Vol. 34, No. 3, 276–280, 1986.

29. Shrestha, S. M. and I. Arai, "Signal processing of ground penetrating radar using spectral estimation techniques to estimate the position of buried targets," *EURASIP J. Appl. Signal Process.*, Vol. 2003, No. 12, 1198–1209, 2003.
30. Iakovleva, E., S. Gdoura, D. Lesselier, and G. Perrusson, "Multistatic response matrix of a 3-D inclusion in half space and MUSIC imaging," *IEEE Trans. Antennas Propag.*, Vol. 55, No. 9, 2598–2609, 2007.
31. Agarwal, K. and X. Chen, "Applicability of MUSIC-type imaging in two-dimensional electromagnetic inverse problems," *IEEE Trans. Antennas Propag.*, Vol. 56, No. 10, 3217–3223, 2008.
32. Abou-Khousa, M. A., D. L. Simms, S. Kharkovsky, and R. Zoughi, "High-resolution short-range wideband FMCW radar measurements based on MUSIC algorithm," *Proc. 2009 IEEE International Instrumentation and Measurement Technology Conf. (I2MTC 2009)*, Singapore, May 2009, DOI: 10.1109/IMTC.2009.5168500.
33. Shirmehenji, F., A. Zeidaabadi-Nezhad, and Z. H. Firouzeh, "Object locating of electromagnetic inclusions in anisotropic permeable background using MUSIC algorithm," *Progress In Electromagnetics Research C*, Vol. 85, 77–89, 2018.